Materials Science & Engineering A 718 (2018) 216–227

Contents lists available at ScienceDirect

Materials Science & Engineering A

journal homepage: www.elsevier.com/locate/msea

Influence of SC-HAZ microstructure on the mechanical behavior of Si-TRIP steel welds

J.J. Guzman-Aguilera[a], C.J. Martinez-Gonzalez[a], V.H. Baltazar-Hernandez[a,*], S. Basak[b], S.K. Panda[b], M.H. Razmpoosh[c], A. Gerlich[c], Y. Zhou[c]

[a] Materials Science and Engineering Department, Autonomous University of Zacatecas, 98000, Mexico
[b] Department of Mechanical Engineering, IIT Kharagpur, Kharagpur 721302, India
[c] Centre for Advanced Materials Joining, University of Waterloo, Canada, N2M 3G1

ARTICLE INFO

Keywords:
Transformation induced plasticity steel
Laser welding
Arc welding
Heat affected zone softening
Carbide precipitation
Formability

ABSTRACT

Transformation induced plasticity (TRIP) steel provides enormous potential for auto-body construction in the automotive sector, owing to its enhanced mechanical behavior. In this work, Si-alloyed TRIP steel is joined by employing laser beam welding (LBW) and by utilizing two arc welding processes: gas tungsten arc welding (GTAW) and gas metal arc welding (GMAW) in order to assess the effect of the net heat input on the microstructure, the uniaxial tensile properties and the forming response. Results indicate that in spite of the Si content in TRIP steel; precipitation and growth of carbides (tempering) are observed in both: the martensite islands and the retained austenite phase, thus leading to the measurable softening at the sub-critical heat affected zone (SC-HAZ) of the arc welded samples. Although the failure location was predominantly found at the sub-critical heat affected zone of the GMAW samples, the maximum stress and elongation was basically controlled by the total extension of the weldment including fusion zone and heat affected zone. While the limiting dome height upon tension-tension (T-T) and tension-compression (T-C) depended primarily on the fusion zone hardness, weld width and geometry of the sample; the fracture location was outside the weld for T-C, whereas the fracture initiated at the weld in T-T samples. LBW specimens showed optimum forming performance.

1. Introduction

Transformation induced plasticity (TRIP) steel belongs to the family of advanced high strength steels (AHSSs) and is composed of a ferrite (α) matrix along with a fraction of retained austenite (γ or RA), dispersed islands of martensite (α′) and some additions of bainite (B) [1]. The relatively high content of Si (i.e. Si-TRIP alloying) and C favors the presence of retained austenite, which in turn promotes an increased hardening rate due to martensite transformation at elevated strains. Such an exceptional structure-property connection is taken into consideration for body-in-white designs where significant stretch forming is required. Furthermore, Si-TRIP steel allows auto makers to meet government regulations concerning both fuel efficiency and passenger safety requirements; thus, making it suitable particularly for crash-worthy behavior in automotive structural components as for example: B-pillar, engine cradle, front and rear rails, among others [1].

In industrial practice, TRIP steel is mainly joined by resistance spot welding (RSW) in the course of assembly [1–8], by laser beam welding (LBW) mostly used in production of tailor-welded blanks [9–12], and by gas metal arc welding (GMAW) in which strength and rigidity is required [13–17]. High fusion zone (FZ) hardness is commonly achieved because of the fast cooling rates encountered by the water-cooling electrodes if employing RSW; however, the joint is prone to fail at the nugget or FZ, in the form of interfacial or partial-interfacial failure mode upon lap-shear tensile testing [2]. The above mentioned failure modes in resistance spot welding of TRIP steel ca n be overcome by employing post-weld heat treatment via a secondary electrode pulse or in-process tempering [3]. On the other hand, penetration, porosity, microstructure, and hardness can be controlled when using LBW in order for the weldment to obtain acceptable mechanical response [9]. For example, a reduction in fusion zone hardness has been obtained when employing twin-spot laser welding [18]. The extent of improvement (once the controlling parameters are set up) has been observed for tailor-welded blanks of dissimilar combinations of advanced high strength steel or mild steel with TRIP steel; for example, excellent fatigue life has been obtained when pairing TRIP steel to mild steel by LBW [10]. Furthermore, the possibility of further controlling the FZ hardness in order to minimize brittleness without losing strength can be

* Correspondence to: Autonomous University of Zacatecas, 801 Ramon Lopez Velarde Ave, 98000 Zacatecas, Mexico.
E-mail address: victor.baltazar@uaz.edu.mx (V.H. Baltazar-Hernandez).

https://doi.org/10.1016/j.msea.2018.01.108
Received 9 October 2017; Received in revised form 25 January 2018; Accepted 25 January 2018

efficiently accomplished by utilizing GMAW; which is attributed to a wide range of filler metals and welding parameter variations available upon this welding process. For instance, the metal inert gas (MIG)-Brazing method with filler metal $ERCuAl_8$ was successfully employed for joining TRIP800 steel thus resulting in comparable strength, lower heat input, reduced zinc evaporation and decreased spatter of the filler metal [13]. Moreover, FZ failures with diminished ultimate tensile strength (i.e. 73% of the weakest alloy) have encountered when attempting to join transformation induced plasticity steel to Twinning-Induced Plasticity steel with an ER307Si filler metal by GMAW process [14].

However, TRIP steel has been hardly studied in the way of employing various welding processes particularly for rating the effect of welding heat input on the resultant fusion zone and/or heat affected zone (HAZ) microstructure, neither to systematically correlate microstructure to its mechanical behavior. For instance, high Si-content TRIP800 steel was laser welded and arc welded by means of metal active gas and tungsten inert gas processes, in the last two employing alloyed filler metal [19]. Although the tensile results indicated that the failure in laser welded sample was located at the base metal (BM) with enhanced ultimate tensile strength (UTS) and an acceptable elongation, the failure switched to the HAZ-BM interface for the arc welded specimens with diminished UTS and clearly reduced ductility [19]. However, in the later report no major details were provided in terms of microstructure development in both fusion zone and heat affected zone. In particular, the effect of softening (tempering) at the SC-HAZ on the tensile properties and the forming characteristics of laser and arc welded TRIP steel.

It is worthy to mention here that another member of the family of AHSS called dual phase (DP) steel is prone to softening at the sub-critical heat affected zone due to tempering of the martensite islands, which has been studied extensively [20–25]. Contrary to this view, scarce communications have been released regarding to softening at the sub-critical heat affected zone of TRIP steels in terms of laser or arc welding processes [26,27]. Zhao et. al. [26] indicated that the reason for softening was the depletion of retained austenite associated with a difference in cooling rates, and to the existence of a large fraction of ferrite but no major discussion was provided. Xia et al. [27] also reported HAZ-softening in diode laser welded TRIP800 steel but no further consideration was given.

This work aims on systematically analyze the influence of fusion zone and sub-critical heat affected zone microstructure on the mechanical response (tensile) and the forming behavior of Si-TRIP steel subjected to different net heat input such as those that involve laser and arc welding.

2. Experimental procedure

2.1. Material

Cold rolled TRIP steel sheet with nominal chemical composition (listed in Table 1), 800 MPa of UTS and thickness of 1.0 mm was used in this study. It is worthy to mention that this type of TRIP steel is also called “Si-TRIP” or “Si-alloyed TRIP” as per the relatively high content of Si [27].

The carbon equivalent as calculated by Yurioka´s equation [28] is $CE_Y = 0.527$. Whereas the corresponding calculated transition temperatures called critical temperatures: Ac_1 and Ac_3 are about 747 °C and 915 °C, respectively. Additionally, the martensite start temperature (M_s) is 380 °C as reported elsewhere [3]. The initial microstructure or base metal microstructure of Si-TRIP steel illustrated in Fig. 1a is composed of a ferrite (α) matrix along with dispersed islands of martensite (α´), retained austenite (γ or RA) with volume fractions of 12–14% and 10–12%, respectively, as per results obtained from metallographic techniques and X–ray diffraction (XRD) analysis (Fig. 1b). In addition, the presence of bainite (B) is also observed in Fig. 1a.

Table 1
Chemical composition of the base metal (wt%).

C	Mn	Si	Cu	Ni	Al	Cr	Mo	P
.18	1.63	1.61	0.02	0.016	0.03	0.02	0.01	0.01

2.2. Welding procedure and heat input

Monolithic Si-TRIP steel sheets were butt-welded by employing three different welding processes: fiber laser welding (LBW), gas tungsten arc welding (GTAW) and gas metal arc welding (GMAW). It has been previously established that heat input increases (from low to high) for the above mentioned welding processes as follows: LBW→GTAW→GMAW [29,30]. Whilst the laser welding process promotes lower heat input; the two arc welding processes represent higher heat input conditions.

LBW samples were made by an *IPG Photonics Ytterbium Doped Fiber YLS-6000* machine operated at 4 kW with a welding speed of 12 m/min, a beam spot size of 600 μm and a focal length of 200 mm. No shielding gas was used during the welding process. GTAW sample was carried out by means of a semiautomatic *Miller Syncrowave™ 250* power source operated at 17.6 kVA / 8.6 kW, employing a pure tungsten type electrode of 1.6 mm in diameter, travel and work angle of 70° and 90°, respectively, and by using direct current electrode negative. GMAW blanks were obtained in an *Infra™ MM 300-E* machine operated at 10.1 kVA / 7.7 kW with non-pulsed short circuit metal transfer mode, using an ER70S-6 solid welding wire of 0.9 mm in diameter, with a travel and work angle of 90°, and by using direct current electrode positive. All welds were made transverse to the rolling direction with zero gap, a series of trials were carried out in order to obtain appropriate welding parameters, all samples were free of any induced visible defects (i.e. lack of fusion, burn-through, porosity, spatter, etc.). Before the welding operation all sheets were fixed in copper-alloy jigs to achieve a heat sink condition in order to minimize further distortion. The optimized parameters for both arc welding processes are provided in Table 2.

Calculations made for the heat input were obtained according to the methodology suggested by Xia et al. [21] through the following equation:

$$\frac{Q_{net}}{vd} = \frac{\rho c (r_{Ac_1} - r_m)(2\pi e)^{1/2}}{\left(\frac{1}{T_{Ac_1} - T_0} - \frac{1}{T_m - T_0}\right)} \quad (1)$$

The net heat input (Q_{net}/vd) as indicated in Eq. (1) representing the thickness normalized net absorbed energy per unit weld length. In this case, ρ is the density of steel, c is the specific heat capacity of steel, r_{Ac1} and r_m are the isotherms positions corresponding to the T_{Ac1} (Ac_1 temperature) and T_m (melting temperature), T_0 is the initial room temperature. The corresponding values of Q_{net}/vd are listed in Table 3.

A physical meaning for the heat input can be properly approached by employing a term called time constant (τ), representing the time to heat a point at the SC-HAZ basically at the lower line of critical temperature Ac_1; hence, high heat input processes require more time to reach the temperature [22].

By assuming that the temperature history during welding is of parabolic shape [25]; and utilizing the method of Xia et al. [21],τ is calculated by means of:

$$\tau = \frac{\left(\frac{Q_{net}}{vd}\right)^2}{4\pi e \rho c_p \lambda (T_{Ac_1} - T_0)^2} \quad (2)$$

where λ is the thermal conductivity.

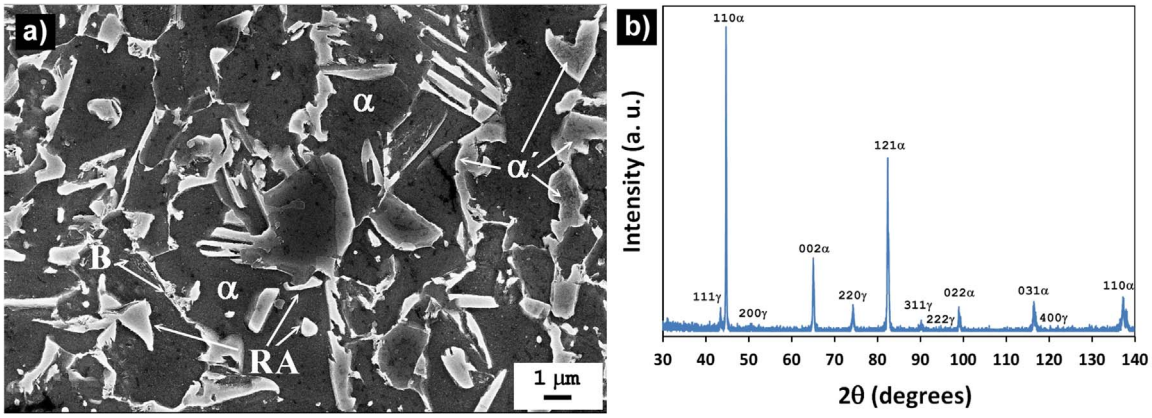

Fig. 1. a) SEM micrograph, and b) XRD pattern of Si-TRIP steel composed of a ferrite matrix (α), islands of martensite (α´), retained austenite phase (γ or RA) and bainite (B).

Table 2
Selected welding parameters for GTAW and GMAW.

Welding Process	Current (A)	Voltage (V)	Shielding Gas	Gas Flow (lt min^{-1})	Travel speed (mm s^{-1})
GTAW	88	28	Ar	13	9.6
GMAW	55	16.5	75% CO_2 + 25% Ar	18	9.6

Table 3
Extension of the different zones of the weldment, net heat input, and time constant.

Sample	Fusion zone (mm)	Heat affected zone (mm)	$\frac{Q_{net}}{vd}$ (J mm^{-2})	τ (s)
LBW	0.5	0.2	6.1	0.01
GTAW	1.8	3.4	80.0	2.2
GMAW	2.6	4.8	92.3	2.9

2.3. Characterization methods

Samples for microstructure and hardness analysis were prepared using standard metallographic procedures followed by etching with 2% Nital solution. Microstructure observations made at the cross-section of all specimens were carried out in an *Olympus*™ BX51M optical microscope. A *Zeiss Ultra Plus* scanning electron microscope (SEM) was utilized for detailed microstructure characterization. Micro X-ray diffraction (Micro-XRD) technique was conducted using Cu-Kα radiation on a *D8Advance Bruker*™ diffractometer, continuous scan mode, in a coupled two-theta-theta scan mode, with a pin of 0.3 mm.

Vickers microhardness measurements were performed along the weldment starting at the fusion zone, extended through the heat affected zone and the base metal using a *Shimadzu*™ HMV hardness tester. The indentation spacing was 200 μm under a testing load of 200 g and dwell time of 15 s. Three sets of indentation lines were obtained through thickness and those were spaced to each other 250 μm. A *Nanovea-M1*™ instrumented indentation machine with a semi-flat tip indenter was employed to assess hardness at the BM and SC-HAZ of the welded specimens [31].

2.4. Uniaxial tensile testing

Base metal tensile specimens were sectioned parallel to the rolling direction, whereas welded specimens were cut perpendicular to the welding direction with the weld line positioned at the center of the gauge length. A *DK-7725e Titanium*™ wire electric discharge machine was employed for machining the final shape and size of all tensile specimens based on ASTM E8/E8M standard. A static condition by setting a crosshead velocity of 2 mm/min was carried out in a *Shimadzu*™ *AG1* universal testing machine.

2.5. Limiting dome height test

Out-of-plane stretch forming setup with a hemispherical punch of 50 mm in diameter was used to evaluate the limiting dome height of the Si-TRIP steel base metal samples as well as the welded samples prepared by different welding processes. A hydraulic press of 100 t capacity was used to attach the stretch forming setup. All the experimental tooling (hemispherical punch, upper and lower die) arrangement is shown elaborately in Fig. 2a. A circular drawbead of 72 mm in diameter was applied on the upper die to clamp the material at the flange region. Utmost care was taken while placing the welded blanks on the lower die as the weld line was always kept exactly at the center of the die opening area. A constant blank holding force of 40 kN was applied and the

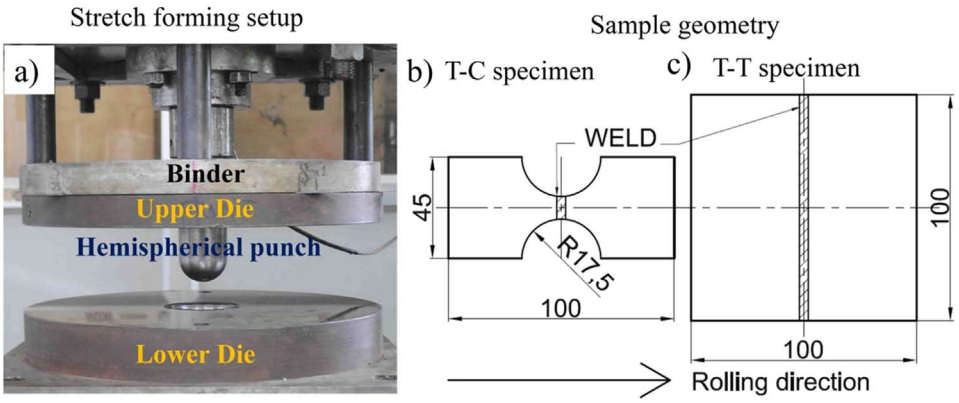

Fig. 2. a) Stretch forming experimental setup with two different sample geometries for achieving b) tension-compression (T-C) and c) tension-tension (T-T) strain path during the limiting dome height test. Displayed dimensions are in mm.

experiment was stopped when necking/fracture was observed in the blank. Maximum dome height up to the visible necking/fracture is termed as limiting dome height. The details of the experimental procedure can be found elsewhere [32–34].

Transverse welded blanks were prepared keeping the weld orientation always perpendicular to the rolling direction of the sheet metal as shown in Fig. 2. Two different geometry samples were designed and subsequently trimmed out from base metal and welded blanks to impart two extremely different strain paths in the specimen during the limiting dome height test. The narrow width specimens as depicted in Fig. 2b were prepared to allow the material flow in the lateral direction during deformation. Hence, tension-compression (T-C) strain path was induced into the narrow specimen while deforming through the test setup. Correspondingly, the narrow width specimen was referred as T-C specimen in this work. Similarly, another square shaped sample with a width greater than the draw bead diameter was prepared as shown in Fig. 2c. This square shaped geometry ensured that the sample was subjected to the tension-tension (T-T) strain path due to biaxial stretching of the specimen. Subsequently, the square specimen was termed as T-T specimen. The T-C specimens were tested in dry condition whereas the T-T specimens were tested in lubricated condition to achieve biaxial tensile strain path. The weld line was strictly kept at the middle of all the T-C and T-T specimens as shown in Fig. 2b and c, respectively. Each experiment was repeated twice for repeatability of the data. The surface of the deforming blanks was etched with circular grid patterns of 2.5 mm in diameter (d_0) through electrochemical etching process. After experiments, the deformed grids were measured along major (d_1) and minor (d_2) axis through optical microscope. The surface strains induced in the specimens were calculated in the logarithmic scale through circular grid analysis (CGA) method [35] using $\varepsilon_i = \ln(d_i/d_0)$ formula, here $i=1,2$ represents major and minor strains respectively. The development of the surface strains or logarithmic strains in various welded samples is discussed in Section 3.

3. Results and discussion

3.1. Microstructure and hardness

Cross-section macrographs showing the path of indentations and the corresponding hardness profile as well as the hardness distribution through thickness along the weldment for LBW, GTAW and GMAW samples are illustrated in Fig. 3a-c. Optical micrographs obtained from different regions such as fusion zone, and heat affected zone at specific zones corresponding to: upper-critical (UC-HAZ), inter-critical (IC-HAZ) and SC-HAZ, are shown in Figs. 4–6, for LBW, GTAW and GMAW, respectively. In addition, Table 3 lists the size of the fusion zone and the heat affected zone for all specimens.

A narrow and relatively hard FZ with formation of columnar grains of martensite is observed in the laser welded sample. The high cooling rates developed upon LBW process clearly resulted in formation of hard martensite phase at the UC-HAZ as well. It is important to mention that presence of lath martensite in both FZ and HAZ in laser welding of transformation induced plasticity steel as a result of the high cooling rates has been reported elsewhere [18,36]. The resultant weld width (Table 3) strongly influenced on the elevated cooling rate that led to formation of predominantly martensite with hardness of 520 ± 17 HV.

In spite of a high volume fraction of martensite in the FZ of the gas tungsten arc welded sample; side-plate ferrite formation is additionally distinguished at the grain boundaries of the solidified columnar structure as indicated with an arrow in Fig. 5a. The presence of ferrite accounts for the reduction of the FZ hardness value of 471 ± 24 HV. Coarse grains of martensite and grain boundary ferrite at the UC-HAZ of the gas tungsten arc welded sample contrast well to fine grains of martensite found at the UC-HAZ of the laser welded samples, (Figs. 4b and 5b). The net heat input in GTAW process promoted a larger weld zone (Table 3) thus resulting in a lower cooling rate, and hence, formation of soft ferrite morphology in both fusion zone and upper-critical heat affected zone.

On the other hand, due to dilution (mixing of chemical composition) between the BM and the filler metal involved in GMAW sample; a high volume fraction of acicular ferrite, side-plate ferrite, widmasttatten ferrite, bainite and some content of martensite are clearly revealed at the FZ as illustrated in Fig. 6a. Due to high heat input as well as the mixed chemistry; the FZ hardness dropped to 291 ± 12 HV (Fig. 3c). Furthermore, martensite, bainite and grain boundary ferrite is observed in the UC-HAZ of gas metal arc welded samples.

Although the inter-critical heat affected zone is quite narrow in LBW sample, it seems higher fraction of martensite, resulted from partial transformation to austenite in heating cycle followed by rapid cooling. On the other hand, no major differences in terms of microstructure at the IC-HAZ were revealed for GMAW and GTAW specimens that were basically composed of ferrite grains along with martensite, bainite, and traces of retained austenite.

So far, the microstructure and hardness of fusion zone, upper-critical and inter-critical heat affected zones seemed predictable according to the inherent heat input of the different welding processes employed. However, it is interesting to note that a considerable drop in hardness value (softening) was markedly measured at the sub-critical heat affected zone of GMAW sample as pointed by the arrow in Fig. 3c. Measurable softening at the SC-HAZ of Si-TRIP steel has been barely reported and no major attention has been received. For instance, a drop in hardness of approximately 75 HV in the SC-HAZ of arc welded TRIP steel was attributed to the existence of a larger volume fraction of ferrite, but in this regard no more details were delivered [26].

In order to further investigate the degree of softening at the sub-critical heat affected zone of TRIP steel, instrumented micro-indentation profiles were obtained for both GTAW and GMAW specimens as shown in Fig. 7. The inset illustrates the localization of the indentation mark just within the SC-HAZ (labeled in both samples as “1”). Based on instrumented indentation results; the displacement of the indenter in both arc welded specimens is clearly larger in comparison to that of the base metal, but markedly larger for the GMAW sample. Consequently, it is further confirmed that GTAW specimen resulted in measurable softening as well; however, the deepest indentation path was observed for the GMAW specimen. Hence, it is confirmed that softening at the sub-critical heat affected zone of TRIP steel was clearly measurable when subjected to arc welding due to tempering of martensite.

It is well established that the isothermal tempering of low-C martensite is developed in various overlapped stages namely: precipitation of carbides, decomposition of retained austenite, coarsening of cementite and recovery of martensite [23,24,37]. Detailed analysis of the sub-critical heat affected zone microstructure for all welded TRIP steel specimens is shown in the SEM micro graphs in Fig. 8c-h (white dashed square within left images is the magnified area of the image on the right), the BM micrograph has also been included as benchmark of the unaffected microstructure (Fig. 8a-b). As a result of the presence of precipitated and growth carbides (presumable of cementite), it is clear that martensite islands undergo tempering at the SC-HAZ of both arc welded specimens (Fig. 8e-h); on the contrary, a very low fraction of extremely fine precipitated carbides are barely observable within the martensite islands in the LBW sample (Fig. 8c-d). The higher heat input applied using the GMAW process resulted in coarser carbides which were preferentially aligned at the prior austenite grain boundaries as well as finer carbides located at the prior block and lathy substructure of the martensite as observed in Fig. 8g-h. It is worth mentioning that in spite of the relatively high content of Si in TRIP steel subjected to rapid thermal cycles below the critical temperature Ac_1, precipitation and growth of carbides at the sub-critical heat affected zone was distinctly found in both arc welding processes.

During tempering, the low solubility of Si within cementite has a significant effect on the growth of carbides [37]. In the early stage of tempering, the growth of cementite is kinetically constrained because

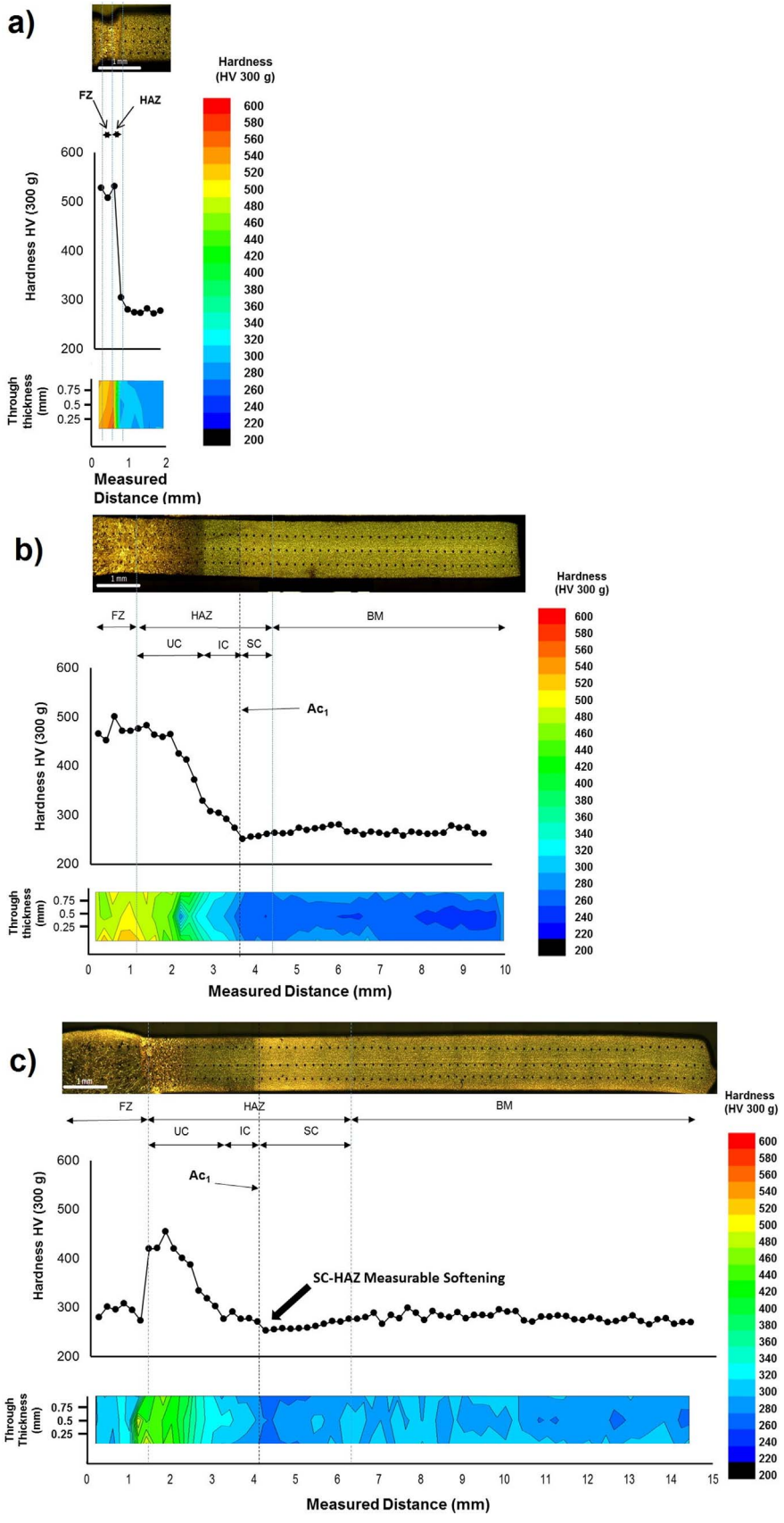

Fig. 3. Cross-section weldment macrograph along with the hardness indentation profile and the distribution of hardness through thickness for: a) LBW, b) GTAW, and c) GMAW specimens, respectively.

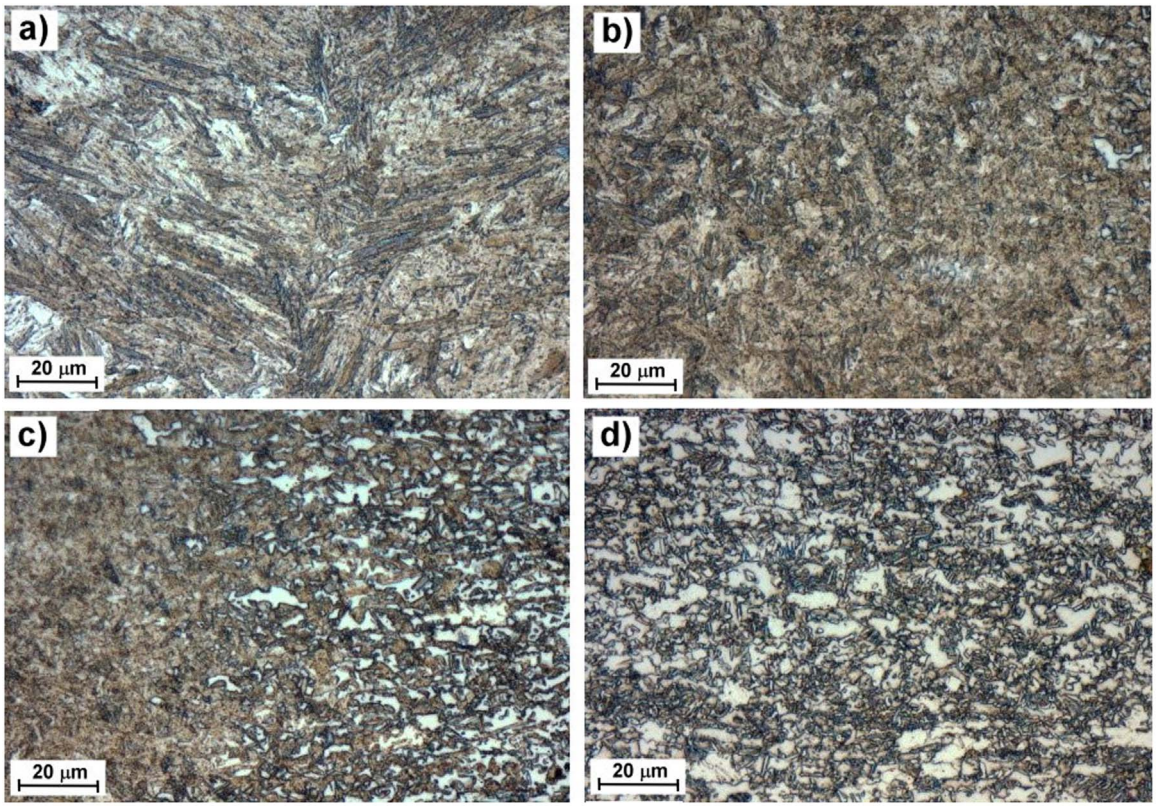

Fig. 4. Microstructure obtained from the LBW specimen at various locations: a) FZ, b) UC-HAZ, c) IC-HAZ and d) SC-HAZ.

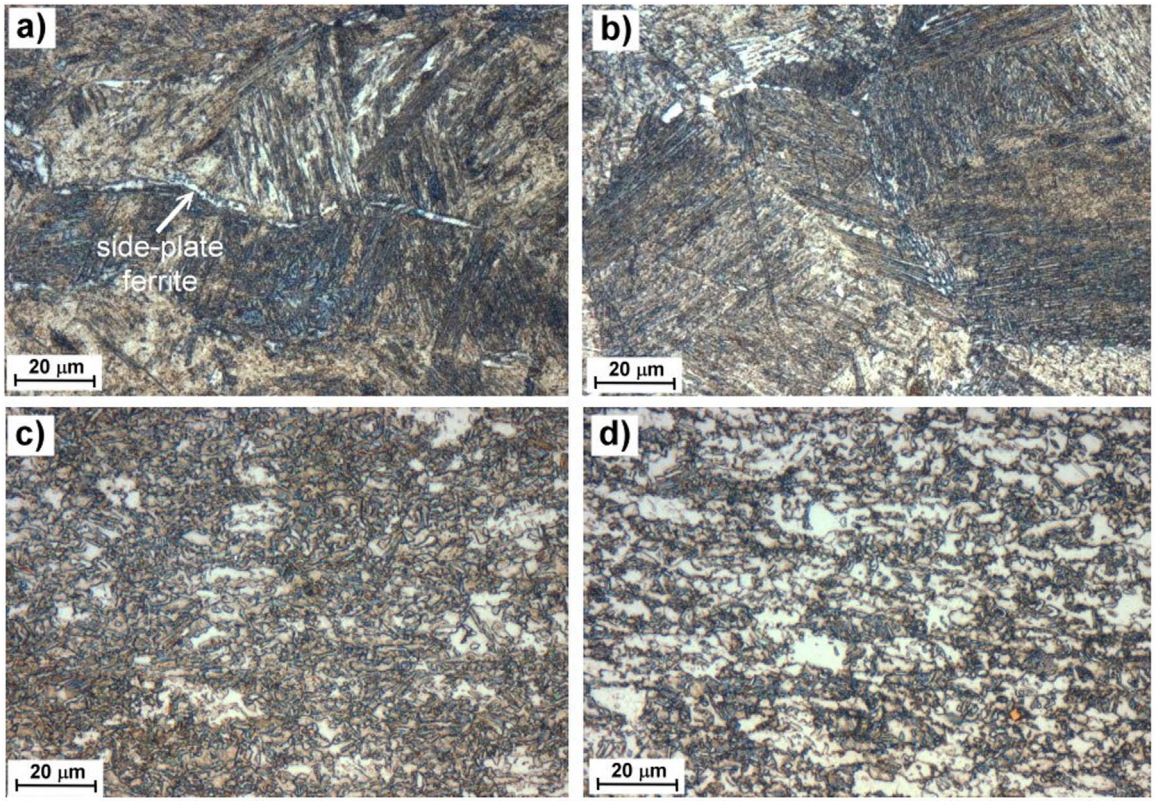

Fig. 5. Microstructure obtained from the GTAW specimen at various locations: a) FZ, b) UC-HAZ, c) IC-HAZ and d) SC-HAZ.

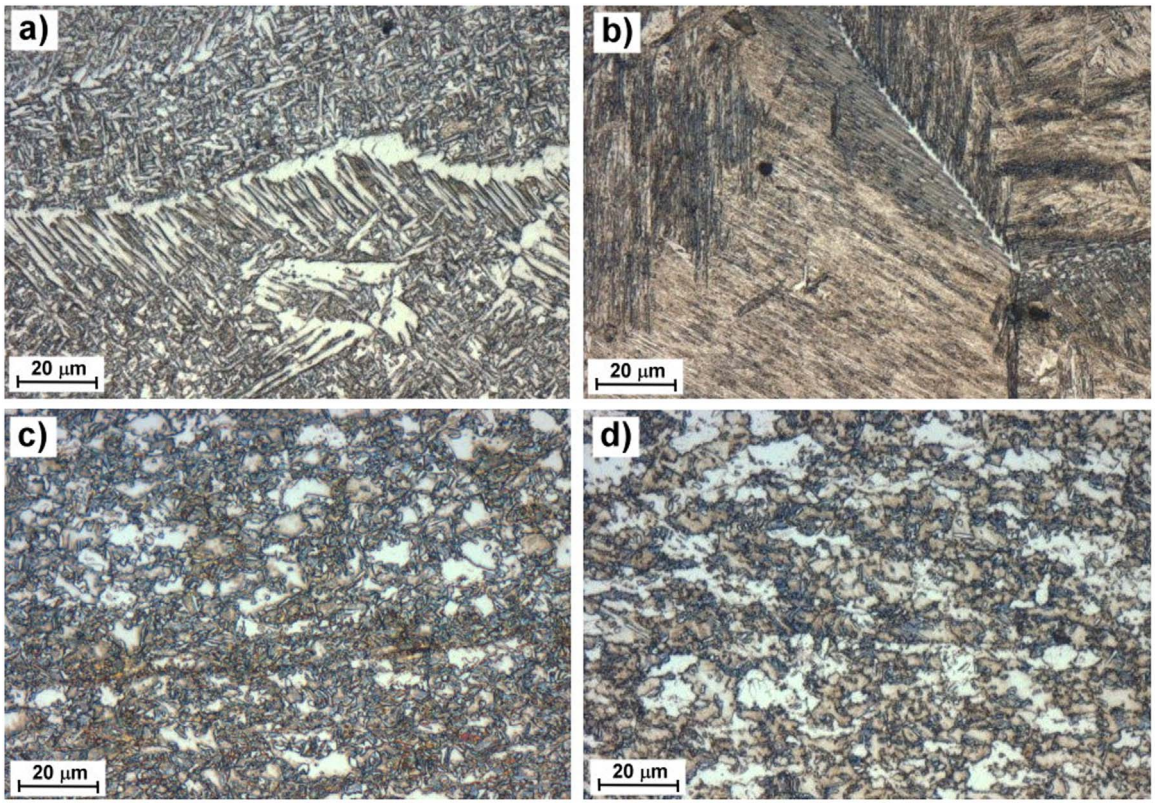

Fig. 6. Microstructure obtained from the GMAW specimen at various locations: a) FZ, b) UC-HAZ, c) IC-HAZ and d) SC-HAZ.

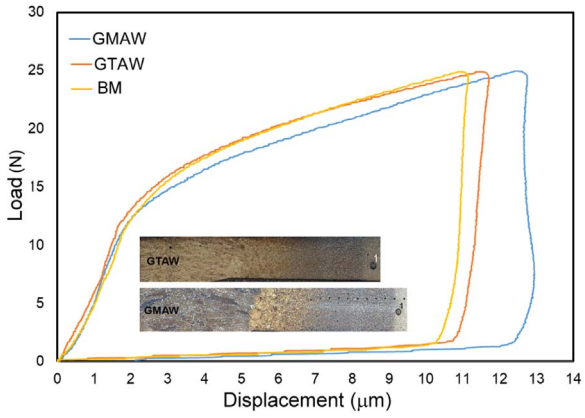

Fig. 7. Instrumented indentation profiles obtained at the SC-HAZ of GTAW and GMAW samples. BM profile has been incorporated for benchmark purpose.

the diffusion of substitutional elements (i.e. Si) is negligible compared to interstitial (C) [38,39]. It has been contended that additions of substitutional Si atoms (~ 2 wt%) modify the tempering characteristics of martensite as it acts as a barrier for cementite growth due to diffusion of Si within the ferrite matrix and further enrichment of the interface ferrite-cementite in the later stages of tempering [40,41]. In this regard, two conditions influence on the retardation of cementite precipitation; a) the overall driving force is drastically reduced because cementite inherits Si from the parent phase and, b) the presence of dislocations reduce the available carbon content for precipitation and growth [38,42]. However, by increasing the peak tempering temperature (i.e. 700 °C); it has been found that Si has less effect in retarding the growth of cementite as compared to Mn, and most of the Si is rejected from cementite even for short period of time [43].

It is worthy to note that by increasing heat input through the various welding processes employed here (LBW→GTAW→ GMAW) increases sub-critical heat affected zone softening (tempering, just beside the Ac_1 line of critical temperature), due to exposure at high temperature for longer times that further permitted the progression of carbide precipitation and growth even in presence of substitutional Si atoms. In earlier practice [22,25,44] the progression of tempering upon welding has been properly modeled by the Johnson-Mehl-Avrami-Kolmogorov (JMAK) equation of transformation as follows:

$$\phi = 1 - \exp(-kt^n) \tag{3}$$

where ϕ represents the fraction of transformation for martensite, k is a fitting parameter representing the energy barrier to transformation, t is the tempering time, and n is the fitting parameter representing the fraction rate. For instance, by assuming a constant k and n and by employing the values obtained for time constant from Table 3 and implying that $\tau = t$, then the progression of transformation resulted higher for GMAW sample, followed by GTAW and finally LBW samples.

Furthermore, if k-value represents the energy barrier for further transformation (nucleation, growth and saturation) and is temperature dependent then can be expressed by Arrhenius expression as follows:

$$k = k_o \exp\left(\frac{-Q}{RT}\right) \tag{4}$$

where k_o is a fitting parameter, Q is the activation energy, R is the universal gas constant and T is temperature. For instance, rich chemistry DP steels have been reported to have reduced k-value as compared to lean chemistry DP steels [22]. Values for k taken from [43] for Fe-C-Si steel are consistent with the previously mentioned. k-value is lower if Si content within the alloy is increased thus reducing the fraction of tempering transformation. However so far, no data is available for precisely separate the effect of increasing Si content in TRIP steel on the ϕ value for different heat input upon welding; hence, further work is required in this regard. Such analysis is beyond this study and will be communicated in future work.

It is worth mentioning that decomposition of retained austenite

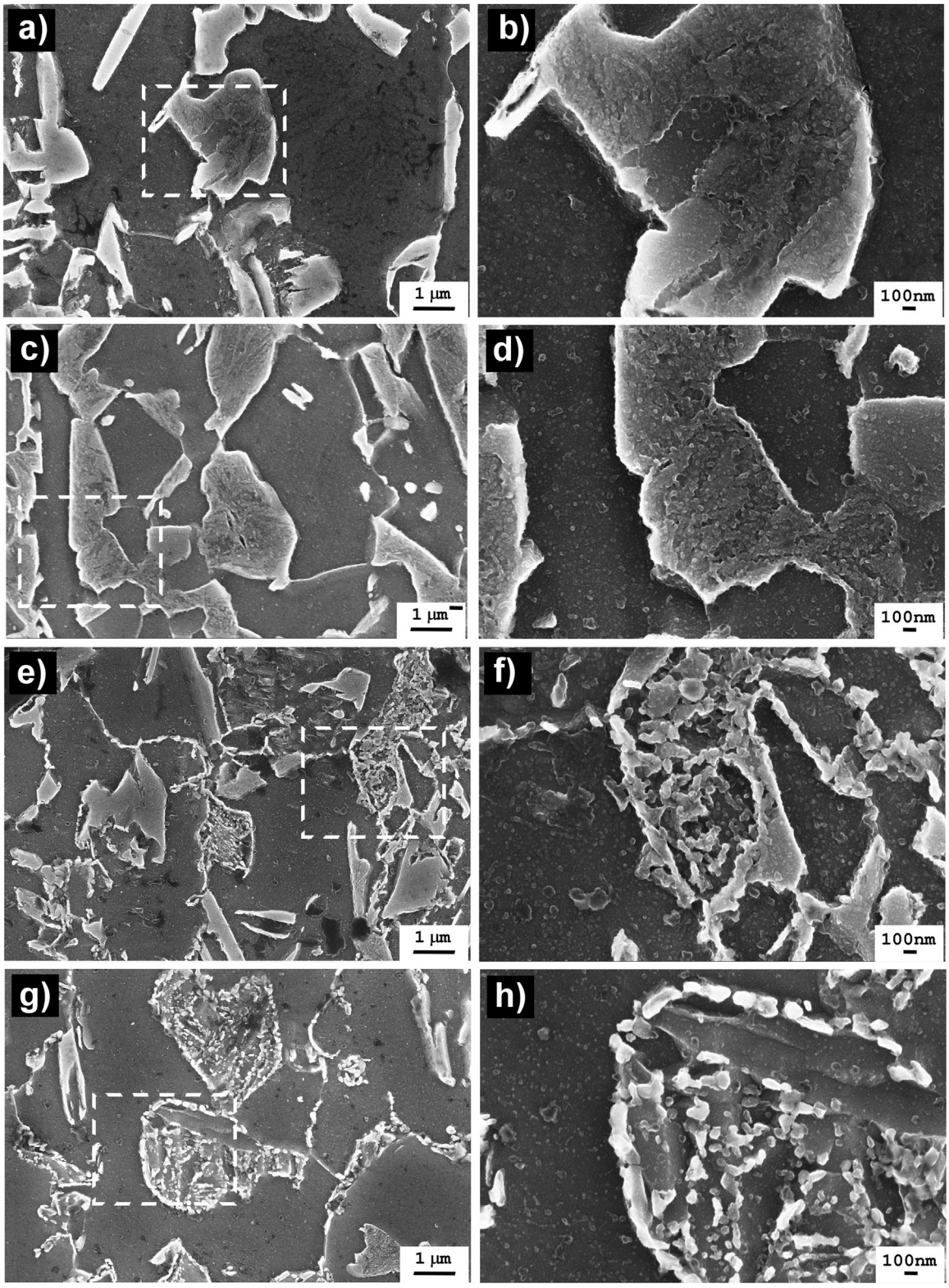

Fig. 8. Detailed SEM microstructure for: a-b) BM, as well as the SC-HAZ microstructure of: c-d) LBW specimen, e-f) GTAW specimen, and g-h) GMAW specimen.

phase (γ or RA) through precipitation of very fine carbides is observed at the sub-critical heat affected zone of GMAW-TRIP steel as shown in the SEM image in Fig. 9a. The corresponding intensity peaks for γ are clearly absent at the XRD pattern in Fig. 9b; thus, confirming that the prior retained austenite phase was further decomposed upon tempering.

It has been stated that in order for cementite to precipitate from its parent retained austenite, an extraordinary long time for the partitioning of Si must be experienced [41]; however, it is important to mention that Si can be ineffective for carbide precipitation if the RA is highly supersaturated with carbon [38]. Carbon-rich RA is an intrinsic characteristic of TRIP-assisted steels because this is promoted by the intercritical annealing and isothermal holding during the bainitic transformation [45]; hence, carbon is available for further precipitation

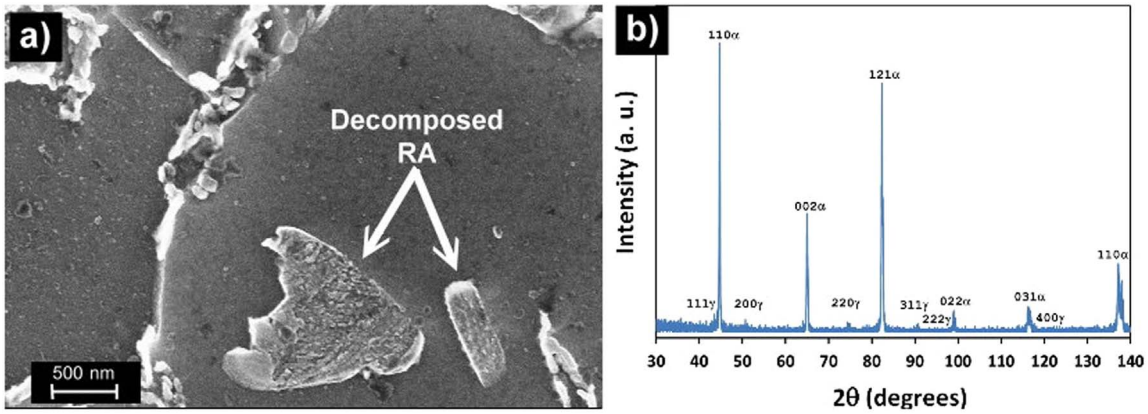

Fig. 9. a) Decomposition of retained austenite (γ or RA) and, b) XRD pattern taken at the SC-HAZ of GMAW specimen.

from austenite during tempering. Consequently, precipitation of cementite from austenite is clearly developed in the Si-TRIP steel because of two reasons; the amount of necessary heat is properly provided by both arc welding processes, and the supersaturation of C within retained austenite.

The presence of large fraction of ferrite as mentioned elsewhere [26] can be properly attributed to the partial-recovery of the lath substructure within the islands of martensite during tempering [23] as depicted in Fig. 8h. The partial-recovery of the ferrite further confirmed that carbide precipitation was favored by the reduction in dislocations and the corresponding trapped carbon available for precipitation [38].

In summary, measurable softening occurring at the sub-critical heat affected zone of high Si-alloyed transformation induced plasticity steel resulted from a combination of various overlapped features: a) the precipitation and coarsening of carbides within the prior islands of martensite, b) the precipitation of supersaturated austenite phase and c) the partial-recovery of the lath structure into the ferrite matrix.

3.2. Uni-axial tensile properties and failure location

The engineering stress-strain curves for base metal and welded specimens are provided in Fig. 10a, the averaged tensile values are accordingly listed in Table 4.

It is clear that by increasing the size of the fusion zone and heat affected zone of the welded specimens (Table 3), the uniform elongation of the sample is undeniably reduced because of the extension of the hard zone; therefore, the displacement within the gauge length of the sample is further restricted. For example, while uniform elongation for LBW was 26% with a FZ of 0.5 mm; it dropped to 20% because the extension of the fusion zone in the GMAW specimen sized 2.6 mm.

Table 4
Experimentally obtained uni-axial tensile properties of base metal and welded specimens.

Sample	YS (MPa)	UTS (MPa)	Uniform Elongation (%)	Total Elongation (%)
BM	559	856	30	37
LBW	562	872	26	31
GTAW	564	863	22	26
GMAW	598	872	20	22

On the other hand, the average of ultimate tensile strength seems to be quite consistent. Accordingly, UTS for all welded specimens were ranging from 863 to 872 MPa; whereas the UTS for the base metal specimen was 856 MPa. The average maximum tensile stress for welded specimens is slightly higher as compared to the BM. Similar results have been previously reported for butt welded TRIP steel [19].

While the failure location for LBW and GTAW specimens consistently resulted at the base metal; it is to be noted that the location of failure was predominantly found at the sub-critical heat affected zone for GMAW samples as depicted by the arrows in Fig. 10b. Although the location of failure can be properly attributed to the degree of tempering occurring at the SC-HAZ of GMAW specimens as described in the previous section; the ultimate tensile strength seemed not influenced by the precipitation and growth of carbides.

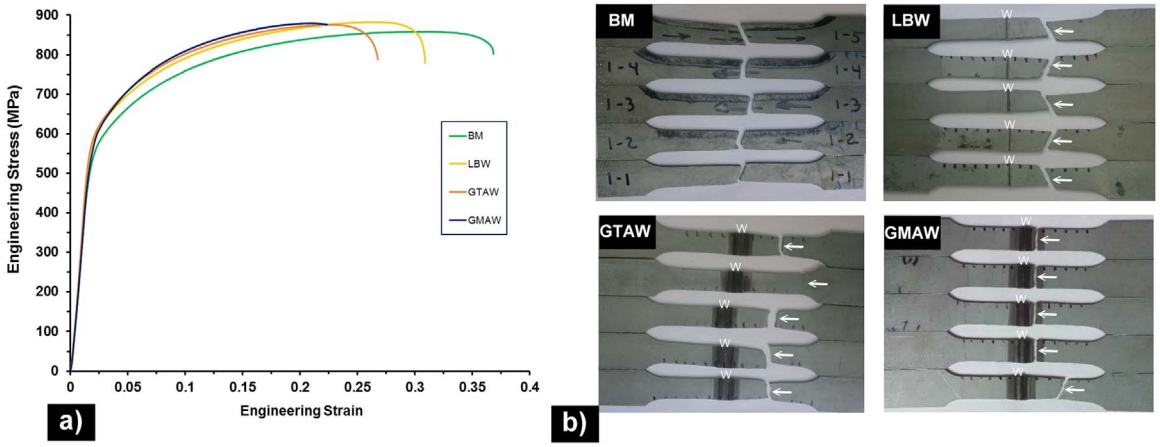

Fig. 10. a) Engineering stress-strain curves and b) fracture location, for BM, LBW, GTAW and GMAW specimens ("W" letter indicates to the location of the fusion zone).

Table 5
Limiting dome height for different welded specimens travelling through different strain path.

Sample	Limiting dome height (mm) of Si-TRIP welded steel prepared by different welding processes			
	BM	LBW	GTAW	GMAW
T-C	7.24 ± 0.08	6.71 ± 0.12	4.95 ± 0.10	5.10 ± 0.08
T-T	23.89 ± 0.24	11.52 ± 0.31	5.17 ± 0.04	9.03 ± 0.17

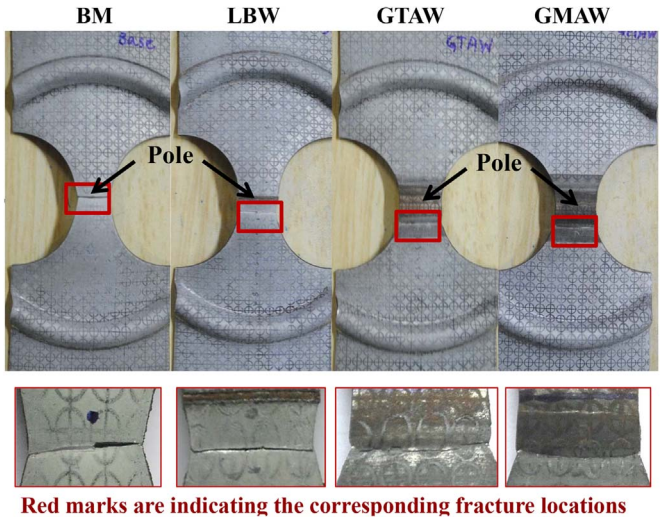

Fig. 11. Fractured tension-compression (T-C) specimens for base material and all the welded Si-TRIP steel specimens with the magnified view of the corresponding fracture locations.

3.3. Formability analysis

3.3.1. Comparison of limiting dome height and fracture location

The limiting dome height was measured with a vernier height gauge with a least count of 0.01 mm. A considerable variation in the limiting dome height was observed for both the T-C and T-T samples as shown in Table 5.

An approximate limiting dome height reduction of 7.3%, 31.6% and 29.6% was recorded for Si-TRIP steel T-C samples prepared by LBW, GTAW and GMAW processes, respectively, as compared to that of T-C base metal samples. The reduction in the limiting dome height is due to the presence of the comparatively harder weld zone as indicated in the macrograph of the various welded specimens as shown in Fig. 3. However, a massive dome height reduction of 51.7%, 78.4% and 62.2% was recorded for Si-TRIP steel T-T samples prepared by LBW, GTAW and GMAW processes respectively compare to that of T-T base samples.

Table 6
Curvilinear distance (in mm) of the fracture location measured from the pole of the deformed sample of Si-TRIP steel prepared by different welding methods.

Sample	BM	LBW	GTAW	GMAW
T-C	0	3.1	5.3	5
T-T	9.5	8	4.2	6.2

Samples prepared by GTAW process exhibited minimum limiting dome height for both of the T-C and T-T condition. The massive reduction in liming dome height for T-T welded specimen was attributed to the presence of harder weld regions and also the shift of the strain path from the extreme biaxial condition to close to plane strain condition for all the welded specimens. It was observed that, the harder weld region was expanded more in longitudinal direction compare to the transverse direction prevailing close to plane strain condition at the weld region. Also, the reduction in the limiting dome height of the welded blanks not only depends on the hardness of the weld but also the width of weld region. For example among the welded samples, Si-TRIP welded steel prepared by laser welding process has the highest weld hardness (520 ± 17 HV) but its fusion zone width is 0.5 mm (Table 3). On the other hand, the weld prepared by gas tungsten arc welding process has comparatively less hardness (471 ± 24 HV) but its span of the FZ is around 1.8 mm. Hence, less deformation was allowed in the T-T sample prepared by GTAW process compare to that of prepared by LBW process till the fracture appears at the weld region. For this reason, limiting dome height of the T-T sample of Si-TRIP steel prepared by GTAW process is much less than the sample prepared by LBW process.

Again, the length of the weld region is less in T-C sample compare to T-T sample. Hence, the effect of the weld is not predominant on the formability of T-C sample. For this reason, the difference in limiting dome height of the T-C samples prepared by LBW process and the base material was very small. However, the limiting dome height was still lesser than the base material, and the failure location was also nearer to the middle of the specimen or pole. Altogether, the formability in terms of limiting dome height of Si-TRIP steel prepared by LBW process is comparatively better than that of prepared by other two welding processes.

It was further observed that, the fracture location of the deformed domes was varied significantly depending on the weld width resulting from different welding processes. The fractured domes with highlighted fracture location for T-C sample and T-T sample were shown in Fig. 11 and Fig. 12, respectively. The topmost point of the dome was termed as the pole as identified in Fig. 11 and Fig. 12. The curvilinear distance of the fracture location from the pole was measured and recorded in Table 6.

For T-C base material of Si-TRIP steel, the fracture was observed exactly at the pole due to the least cross sectional area of the sample at that location. However, the fracture shifts from the pole for the welded

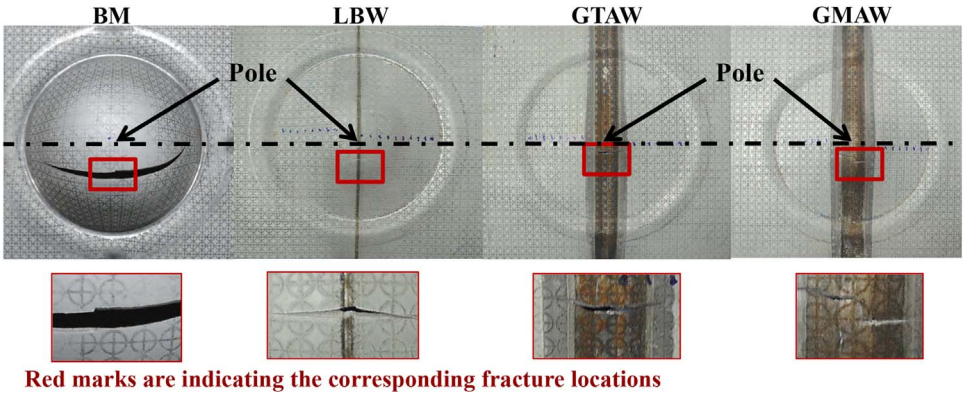

Fig. 12. Fractured tension-tension (T-T) specimens for base sample and all the welded Si-TRIP steel samples with the magnified view of the corresponding fracture locations.

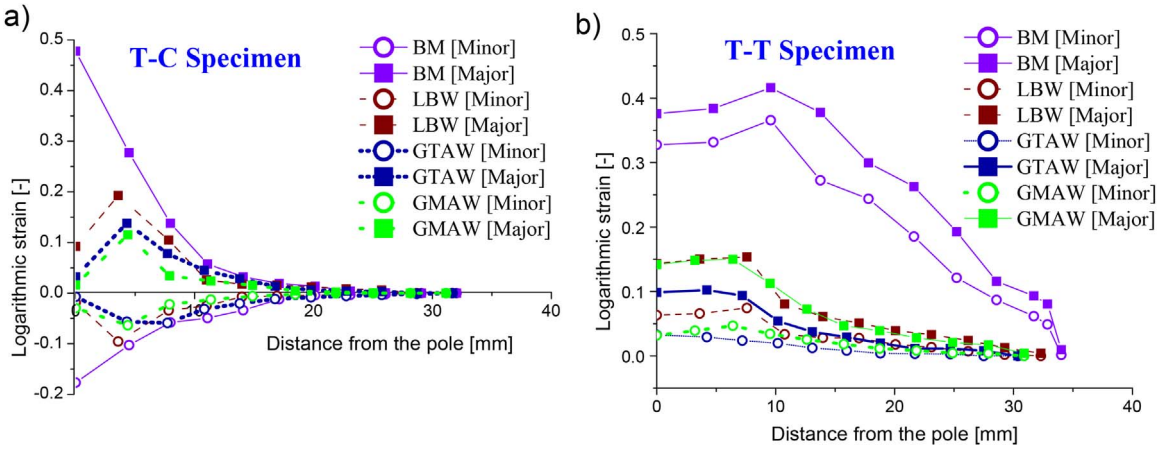

Fig. 13. Strain distribution profile for deformed specimen with different weld conditions for a) tension-compression (T-C) and b) tension-tension (T-T) strain path.

T-C sample of Si-TRIP steel. This shifting depends upon the width of the weld region. The fracture location is nearly same for both T-C samples prepared by both arc welding processes. It is observed that, the failure location is outside of the heat affected zone region for T-C sample prepared by GTAW process.

On contrary, the failure location is inside the sub-critical heat affected zone softening region for T-C sample prepared by gas metal arc welding process. For T-T sample, the fracture on the base materials was recorded parallel to the rolling direction. The fracture was always initiated from the welded region and then propagated to the base materials for the welded T-T sample. The fracture was always recorded across the weld as shown explicitly in the inset of the Fig. 12.

3.3.2. Strain distribution profiles

Major and minor logarithmic strains were measured across the weld along the rolling direction for the deformed samples of the base materials and welded samples. Consequently, the strain distribution profiles are shown for both T-C sample (Fig. 13a) and T-T sample (Fig. 13b). The strain distribution profiles are approximately symmetric along the weld line. Hence, half symmetry strain distribution profiles are shown in Fig. 13.

Maximum major and minimum minor strain was observed at the pole of the T-C base material. Whereas for welded T-C samples, the maximum major strain was observed at a certain distance from the pole. The strain profiles of T-C samples prepared by both arc welding processes are quite similar. The major strain for T-C sample prepared by LBW process is higher than that of the T-C sample prepared by GTAW and GMAW processes. All these strain profiles were analogous to the limiting dome height test data and the failure location of the T-C samples. It is further observed from Fig. 13b that, the major and minor strain distribution profiles of the base material are very close to each other. This confirms the biaxial tensile strain path was achieved during the deformation of the base T-T samples. However, the difference between the major and minor strain profiles is more in case of T-T samples prepared by LBW, GTAW and GMAW processes, and the maximum minor strain is nearly 0.1 for all of them. Hence, the deformation mode approached closer towards the plane strain condition in all the welded samples.

Also, it is well established that the limiting strain is minimal at the plane strain condition of a sheet material forming operation [46,47]. This explains the massive reduction in the formability of the welded blank as confirmed from the limiting dome height test data. The lowest overall major strain profile was recorded for T-T sample prepared by the gas tungsten arc welding process.

4. Conclusions

In this work, the influence of the fusion zone and the sub-critical heat affected zone microstructure on the mechanical response (tensile) and the forming behavior of Si-TRIP steel subjected to different net heat input such as those that involve laser and arc welding has been systematically analyzed, from which the following conclusions can be addressed.

1. The measurable softening (tempering) occurring at the sub-critical heat affected zone of arc welded Si-TRIP steel resulted from a combination of various overlapped metallurgical processes: a) the precipitation and coarsening of carbides within the prior islands of martensite, b) the precipitation of supersaturated austenite phase and c) the partial-recovery of the lath substructure of martensite. The degree of softening (just beside the Ac_1 line of critical temperature) was depending upon the increased heat input through the various welding processes employed here as follows: LBW (non-measurable) →GTAW (measurable) →GMAW (clearly measurable).
2. Ductility upon uniaxial tensile testing was evidently influenced by the total size of the fusion zone and the heat affected zone. It has been observed that the uniform elongation was further reduced for both arc welded specimens. However, the maximum strength seemed not to be affected significantly by size of both the FZ and HAZ. In contrast, all welded specimens actually registered slightly higher values of UTS. The location of failure was observed in the BM of both LBW and GTAW specimens; interestingly, the failure location was predominantly encountered at the sub-critical heat affected zone of the gas metal arc welded TRIP steel, clearly attributed to the degree of softening.
3. Formability of Si-TRIP welded steel depends on the weld hardness, weld width and geometry of the specimen. For T-C specimen the fracture always took place outside of the weld width whereas the fracture was initiated at the weld region in case of T-T specimen. Strain path was changed from extreme biaxial condition towards close to plane strain condition while deforming T-T welded specimen. Also the weld zone is harder comparatively to the base material. Therefore a huge reduction of the limiting dome height for T-T welded specimen were recorded, whereas the limiting dome height reduction was comparatively minimal for T-C welded specimen compare to that of the corresponding base materials. Among the welded blanks, the blank prepared by LBW process showed maximum formability in terms of limiting dome height followed by the other two welded blanks prepared by the GMAW and GTAW processes for both of the sample geometry.

Acknowledgements

J.J. Guzman-Aguilera wants to thank the Mexican National Council of Science and Technology (CONACYT-Mexico) for providing the funding for this research project. Also, J.J. Guzman-Aguilera wants to thank Abdelbaset Midawi from University of Waterloo Canada for assisting with the instrumented indentation tests. V.H. Baltazar-Hernandez wants to acknowledge CONACYT INFRA-2015-254731 project for funding the XRD laboratory facilities.

References

[1] S. Keeler, M. Kimchi, P.J. Mooney, Advanced High-Strength Steels Apllication Guidelines Version 6.0. 〈http://www.worldautosteel.org/download_files/AHSSGuidelinesV6/00_AHSSGuidelines_V6_20170430.pdf〉, 2017.

[2] N. den Uijl, S. Smith, C. Goos, E. van der Aa, T. Moolevliet, T. van der Veldt, Failure modes of resistance spot welded advanced high strength steels, in: D.W. Zhang, N. Scotchmer (Eds.), Proc. 5th Int. Semin. “Advances Resist. Welding”, Toronto, Canada, Toronto, ON, pp. 78–104. 〈https://www.swantec.com/about-us/events/〉, 2008.

[3] V.H. Baltazar Hernandez, Y. Okita, Y. Zhou, Second pulse Current in resistance spot welded TRIP steel – effects on the microstructure and mechanical behavior, Weld. J. 91 (2012) 278S–285S 〈https://app.aws.org/wj/supplement/WJ_2012_10_s278.pdf〉.

[4] S. Brauser, L.A. Pepke, G. Weber, M. Rethmeier, Deformation behaviour of spot-welded high strength steels for automotive applications, Mater. Sci. Eng. A 527 (2010) 7099–7108, http://dx.doi.org/10.1016/j.msea.2010.07.091.

[5] T.B. Hilditch, J.G. Speer, D.K. Matlock, Effect of susceptibility to interfacial fracture on fatigue properties of spot-welded high strength sheet steel, Mater. Des. 28 (2007) 2566–2576, http://dx.doi.org/10.1016/j.matdes.2006.10.019.

[6] X. Sun, E.V. Stephens, M.A. Khaleel, Effects of fusion zone size and failure mode on peak load and energy absorption of advanced high strength steel spot welds under lap shear loading conditions, Eng. Fail. Anal. 15 (2008) 356–367, http://dx.doi.org/10.1016/j.engfailanal.2007.01.018.

[7] S. Dancette, D. Fabrègue, V. Massardier, J. Merlin, T. Dupuy, M. Bouzekri, Investigation of the tensile shear fracture of advanced high strength steel spot welds, Eng. Fail. Anal. 25 (2012) 112–122, http://dx.doi.org/10.1016/j.engfailanal.2012.04.009.

[8] V.H. Baltazar Hernandez, M.L. Kuntz, M.I. Khan, Y. Zhou, Influence of microstructure and weld size on the mechanical behaviour of dissimilar AHSS resistance spot welds, Sci. Technol. Weld. Join. 13 (2008) 769–776, http://dx.doi.org/10.1179/136217108X325470.

[9] T.-K. Han, S.S. Park, K.-H. Kim, C.-Y. Kang, I.-S. Woo, J.-B. Lee, CO_2 laser welding characteristics of 800 MPa class TRIP steel, ISIJ Int. 45 (2005) 60–65, http://dx.doi.org/10.2355/isijinternational.45.60.

[10] R.S. Sharma, P. Molian, Yb:YAG laser welding of TRIP780 steel with dual phase and mild steels for use in tailor welded blanks, Mater. Des. 30 (2009) 4146–4155, http://dx.doi.org/10.1016/j.matdes.2009.04.033.

[11] N. Lun, D.C. Saha, A. Macwan, H. Pan, L. Wang, F. Goodwin, Y. Zhou, Microstructure and mechanical properties of fibre laser welded medium manganese TRIP steel, Mater. Des. 131 (2017) 450–459, http://dx.doi.org/10.1016/j.matdes.2017.06.037.

[12] A. Grajcar, M. Rózański, M. Kamińska, B. Grzegorczyk, Effect of gas atmosphere on the non-metallic inclusions in laser-welded trip steel with Al and Si additions, Mater. Tehnol. 50 (2016) 945–950, http://dx.doi.org/10.17222/mit.2015.253.

[13] F. Varol, E. Ferik, U. Ozsarac, S. Aslanlar, Influence of current intensity and heat input in Metal Inert Gas-brazed joints of TRIP 800 thin zinc coated steel plates, Mater. Des. 52 (2013) 1099–1105, http://dx.doi.org/10.1016/j.matdes.2013.06.054.

[14] K. Májlinger, E. Kalácska, P. Russo Spena, Gas metal arc welding of dissimilar AHSS sheets, Mater. Des. 109 (2016) 615–621, http://dx.doi.org/10.1016/j.matdes.2016.07.084.

[15] M. Zhang, L. Li, R. Fu, J. Zhang, Z. Wan, Weldability of low carbon transformation induced plasticity steel, J. Iron Steel Res. Int. 15 (2008) 61–65, http://dx.doi.org/10.1016/S1006-706X(08)60250-2.

[16] E. Biro, C. Jiang, J. Hunt, LME and Hot Cracking Sensitivity of AHSS during Gas Metal Arc Welding and Brazing, in: Sheet Met. Weld. Conference XIV, Livonia, MI, pp. 1–13. 〈http://www.awsdetroit.org/smwc.html〉, 2010.

[17] M. Shome, M. Tumuluru, Welding and joining of advanced high strength steels, 2015th ed., Woodhead Publishing, Sawston, Cambridge, 2015〈https://www.elsevier.com/books/welding-and-joining-of-advanced-high-strength-steels-ahss/shome/978-0-85709-436-0〉.

[18] A. Grajcar, B. Grzegorczyk, M. Rózański, S. Stano, M. Morawiec, Microstructural aspects of bifocal laser welding of trip steels, Arch. Metall. Mater. 62 (2017) 611–618, http://dx.doi.org/10.1515/amm-2017-0090.

[19] S. Němeček, T. Mužík, M. Míšek, Differences between laser and arc welding of HSS steels, Phys. Procedia 39 (2012) 67–74, http://dx.doi.org/10.1016/j.phpro.2012.10.015.

[20] D.C. Saha, D. Westerbaan, S.S. Nayak, E. Biro, A.P. Gerlich, Y. Zhou, Microstructure-properties correlation in fiber laser welding of dual-phase and HSLA steels, Mater. Sci. Eng. A 607 (2014) 445–453, http://dx.doi.org/10.1016/j.msea.2014.04.034.

[21] M. Xia, E. Biro, Z. Tian, Y.N. Zhou, Effects of heat input and martensite on HAZ softening in laser welding of dual phase steels, ISIJ Int. 48 (2008) 809–814, http://dx.doi.org/10.2355/isijinternational.48.809.

[22] E. Biro, J.R. McDermid, J.D. Embury, Y. Zhou, Softening kinetics in the subcritical heat-affected zone of dual-phase steel welds, Metall. Mater. Trans. A Phys. Metall. Mater. Sci. 41 (2010) 2348–2356, http://dx.doi.org/10.1007/s11661-010-0323-2.

[23] V.H. Baltazar Hernandez, S.S. Nayak, Y. Zhou, Tempering of martensite in dual-phase steels and its effects on softening behavior, Metall. Mater. Trans. A Phys. Metall. Mater. Sci. 42 (2011) 3115–3129, http://dx.doi.org/10.1007/s11661-011-0739-3.

[24] S.S. Nayak, V.H. Baltazar Hernandez, Y. Zhou, Effect of chemistry on nonisothermal tempering and softening of dual-phase steels, Metall. Mater. Trans. A Phys. Metall. Mater. Sci. 42 (2011) 3242–3248, http://dx.doi.org/10.1007/s11661-011-0868-8.

[25] E. Biro, S. Vignier, C. Kaczynski, J.R. Mcdermid, E. Lucas, J.D. Embury, Y.N. Zhou, Predicting transient softening in the sub-critical heat-affected zone of dual-phase and martensitic steel welds, ISIJ Int. 53 (2013) 110–118, http://dx.doi.org/10.2355/isijinternational.53.110.

[26] L. Zhao, M.K. Wibowo, M.J.M. Hermans, S.M.C. van Bohemen, J. Sietsma, Retention of austenite in the welded microstructure of a 0.16C-1.6Mn-1.5Si (wt%) TRIP steel, J. Mater. Process. Technol. 209 (2009) 5286–5292, http://dx.doi.org/10.1016/j.jmatprotec.2009.03.017.

[27] M. Xia, Z. Tian, L. Zhao, Y.N. Zhou, Metallurgical and mechanical properties of fusion zones of TRIP steels in laser welding, ISIJ Int. 48 (2008) 483–488, http://dx.doi.org/10.2355/isijinternational.48.483.

[28] N. Yurioka, H. Suzuki, S. Ohshita, S. Saito, Determination of necessary preheating temperature in steel welding, Weld. J. 62 (1983) 147–153 〈https://app.aws.org/wj/supplement/WJ_1983_06_s147.pdf〉.

[29] J.H. Lee, S.H. Park, H.S. Kwon, G.S. Kim, C.S. Lee, Laser, tungsten inert gas, and metal active gas welding of DP780 steel: comparison of hardness, tensile properties and fatigue resistance, Mater. Des. 64 (2014) 559–565, http://dx.doi.org/10.1016/j.matdes.2014.07.065.

[30] Q. Sun, H.-S. Di, J.-C. Li, B.-Q. Wu, R.D.K. Misra, A comparative study of the microstructure and properties of 800 MPa microalloyed C-Mn steel welded joints by laser and gas metal arc welding, Mater. Sci. Eng. A 669 (2016) 150–158, http://dx.doi.org/10.1016/j.msea.2016.05.079.

[31] A.R.H. Midawi, C.H.M. Simha, A.P. Gerlich, Novel techniques for estimating yield strength from loads measured using nearly-flat instrumented indenters, Mater. Sci. Eng. A 675 (2016) 449–453, http://dx.doi.org/10.1016/j.msea.2016.08.056.

[32] S.S. Hecker, A cup test for assesing stretchability, Met. Eng. Q. 14 (1974) 30–36 〈https://www.scopus.com/inward/record.url?eid=2-s2.0-0016126252&partnerID=10&rel=R3.0.0〉.

[33] S. Basak, S.K. Panda, Implementation of Yld96 anisotropy plasticity theory for estimation of polar effective plastic strain based failure limit of pre-strained thin steels, Thin-Walled Struct. (2016) 1–12, http://dx.doi.org/10.1016/j.tws.2017.04.015.

[34] S. Dhara, S. Basak, S.K. Panda, S. Hazra, B. Shollock, R. Dashwood, Formability analysis of pre-strained AA5754-O sheet metal using Yld96 plasticity theory: role of amount and direction of uni-axial pre-strain, J. Manuf. Process. 24 (2016) 270–282, http://dx.doi.org/10.1016/j.jmapro.2016.09.014.

[35] S. Basak, K. Bandyopadhyay, S.K. Panda, P. Saha, Prediction of formability of Bi-axial pre-strained dual phase steel sheets using stress-based forming limit diagram, in: R.G. Narayanan, U.S. Dixit (Eds.), Adv. Mater. Form. Join. Springer, 2015, pp. 167–192, , http://dx.doi.org/10.1007/978-81-322-2355-9.

[36] A. Grajcar, M. Morawiec, M. Różański, S. Stano, Twin-spot laser welding of advanced high-strength multiphase microstructure steel, Opt. Laser Technol. 92 (2017) 52–61, http://dx.doi.org/10.1016/j.optlastec.2017.01.011.

[37] G.R. Speich, W.C. Leslie, Tempering of steel, Metall. Trans. 3 (1972) 1043–1054, http://dx.doi.org/10.1007/BF02642436.

[38] E. Kozeschnik, H.K.D.H. Bhadeshia, Influence of silicon on cementite precipitation in steels, Mater. Sci. Technol. 24 (2008) 343–347, http://dx.doi.org/10.1179/174328408X275973.

[39] G. Ghosh, G.B. Olson, Precipitation of paraequilibrium cementite: experiments, and thermodynamic and kinetic modeling, Acta Mater. 50 (2002) 2099–2119, http://dx.doi.org/10.1016/S1359-6454(02)00054-X.

[40] S.S. Babu, K. Hono, T. Sakurai, APFIM studies on martensite tempering of Fe-C-Si-Mn low alloy steel, Appl. Surf. Sci. 67 (1993) 321–327, http://dx.doi.org/10.1016/0169-4332(93)90333-7.

[41] F. Tariq, N. Naz, R.A. Baloch, A. Ali, Evolution of microstructure and mechanical properties during quenching and tempering of ultrahigh strength 0.3C Si-Mn-Cr-Mo low alloy steel, J. Mater. Sci. 45 (2010) 1695–1708, http://dx.doi.org/10.1007/s10853-009-4160-x.

[42] W.J. Nam, C.M. Bae, Coarsening behavior of cementite particles at a subcritical temperature in a medium carbon steel, Scr. Mater. 41 (1999) 313–318, http://dx.doi.org/10.1016/S1359-6462(99)00168-2.

[43] G. Miyamoto, J.C. Oh, K. Hono, T. Furuhara, T. Maki, Effect of partitioning of Mn and Si on the growth kinetics of cementite in tempered Fe-0.6 mass% C martensite, Acta Mater. 55 (2007) 5027–5038, http://dx.doi.org/10.1016/j.actamat.2007.05.023.

[44] E. Biro, J.R. McDermid, S. Vignier, Y. Norman Zhou, Decoupling of the softening processes during rapid tempering of a martensitic steel, Mater. Sci. Eng. A. 615 (2014) 395–404, http://dx.doi.org/10.1016/j.msea.2014.07.102.

[45] P.J. Jacques, E. Girault, A. Mertens, B. Verlinden, J. Van Humbeeck, F. Delannay, The developments of cold-rolled TRIP-assisted multiphase steels. Al-alloyed TRIP-assisted multiphase steels, ISIJ Int. 41 (2001) 1068–1074, http://dx.doi.org/10.2355/isijinternational.41.1068.

[46] S. Basak, S.K. Panda, Y.N. Zhou, Formability assessment of prestrained automotive grade steel sheets using stress based and polar effective plastic strain-forming limit diagram, J. Eng. Mater. Technol. 137 (2015) 41006–41012, http://dx.doi.org/10.1115/1.4030786.

[47] D. Banabic, H.-J. Bunge, K. Pöhlandt, A.E. Tekkaya, Formability of Metallic Materials: Plastic Anisotropy, Formability Testing, Forming Limits, 1st ed., Springer-Verlag Berlin, Heidelberg, 2000, http://dx.doi.org/10.1007/978-3-662-04013-3.